ADVANCED FUNCTIONAL MATERIALS
www.afm-journal.de

Surface Regulation through Dipolar Molecule Boosting the Efficiency of Mixed 2D/3D Perovskite Solar Cell to 24%

*Xiaopeng Yue, Xing Zhao, Bingbing Fan, Yingying Yang, Luyao Yan, Shujie Qu, Hao Huang, Qiang Zhang, Huilin Yan, Peng Cui, Jun Ji, Junfeng Ma, and Meicheng Li**

Mixed 2D/3D perovskite solar cells (PSCs) show promising performances in efficiency and long-term stability. The functional groups terminated on a large organic molecule used to construct 2D capping layer play a key role in the chemical interaction mechanism and thus influence the device performance. In this study, 4-(trifluoromethyl) benzamidine hydrochloride (TFPhFACl) is adopted to construct 2D capping layer atop 3D perovskite. It is found that there are two mechanisms synergistically contributing to the increase of efficiency: 1) The $TFPhFA^+$ cations form a dipole layer promoting the interfacial charge transport. 2) The suppressed nonradiative recombination of perovskite through the coordination of $TFPhFA^+$ cations with Pb–I octahedron, as well as the recrystallization of 3D perovskite induced by Cl^- ions. As a result, the PSC delivers an efficiency of 24.0% with improved open-circuit voltage (V_{OC}) of 1.16 V, short-circuit current density (J_{SC}) of 25.42 mA cm^{-2}, and fill factor of 81.26%. The device shows no decrease in efficiency after 1500 h stored in the air indicating the good stability. The utilization of TFPhFACl not only provides a facile way to optimize the interfacial problems, but also gives a new perspective for rational design of large spacer molecule for constructing efficient 2D/3D PSCs.

1. Introduction

Organic–inorganic perovskite solar cells (PSCs) have emerged as a rising star in the photovoltaic area owning to their high-efficiency and easy-fabrication process.[1–3] In the past decade, the PSCs have made a remarkable breakthrough with a certified power conversion efficiency (PCE) of 25.7%.[4] Traditional 3D perovskites using small organic cations such as $CH_3NH_3^+$, $CH(NH_2)_2^+$, and Cs^+ suffer severe interfacial problems such as energy level mismatch, and trap defects induced nonradiative recombination.[5,6] Surface treatment of 3D perovskite with 2D perovskite is an effective way to improve device efficiency through regulating the band alignment, passivating the trap defects, and modulating the film quality of 3D perovskite.[7–12]

Large organic spacer group functionalized with amines has been widely used to construct 2D capping layer. Compared with amine groups, formamidinium group has stronger interaction with Pb–I octahedron and faster charge transport properties.[13] Up to now, there are a few reports using formamidinium derivates to fabricate 2D perovskite layer. Formamidinium derivates, such as 2-thiophenefor-mamidinium (ThFA), aromatic formamidinium (PhFA and p-FPhFA), have been reported by the same group and used as light absorbers in quasi-2D PSCs.[14,15] Chloro-phenylformamidinium ($CPFA^+$) spacer cation was also investigated by Li et al., and the quasi-2D PSC has a PCE of 14.78% with good ambient stability.[16] Incorporation of small amount of aromatic formamidinium into bulk 3D perovskite is one way to enhance the device efficiency.[17] Although the PSCs using aromatic FA-based 2D or quasi-2D perovskites show excellent stability, the photovoltaic performances still lag far behind their 3D counterparts due to the poor conductivity, wide optical bandgap and higher exciton binding energy.[18–20] Thus, it is of great importance to balance the efficiency and stability of PSCs, and integrating the advantages of 2D and 3D perovskites paves a new way to achieve this goal.

Introducing interfacial dipole layer has been one of the popular strategies for PSCs in surface engineering.[21,22] An interfacial dipole can shift the electronic band structure and thus tunes the charge transport. 2D perovskite azetidinium lead iodide ($AzPbI_3$) was found to induce a dipole interlayer between perovskite and hole transport material that promotes the charge transport.[23] Other organic materials such as ortho-fluorinated phenethylamine (2-F-PEAI), 2,2,2-trifluoroethylamine (F_3EAI), and aniline derivant have been successfully applied to the PSCs to adjust the surface electronic structure.[24–26] In order to increase the molecular dipole moments, functional groups with large electronegativity are preferred, such as Cl, F or CF_3 groups, which will influence the interfacial carrier extraction kinetics.[15,27,28] Therefore, to construct an effective 2D capping layer, a rational design of molecular structure with proper

X. Yue, X. Zhao, B. Fan, Y. Yang, L. Yan, S. Qu, H. Huang, Q. Zhang, H. Yan, P. Cui, J. Ji, J. Ma, M. Li
State Key Laboratory of Alternate Electrical Power System with Renewable Energy Sources, School of New Energy
North China Electric Power University
Beijing 102206, China
E-mail: mcli@ncepu.edu.cn
X. Yue
School of Energy and Environmental Engineering
Hebei University of Engineering
Handan, Hebei 056038, China
The ORCID identification number(s) for the author(s) of this article can be found under https://doi.org/10.1002/adfm.202209921.

DOI: 10.1002/adfm.202209921

functional groups is necessary, which can have a significant effect on the surface passivation mechanism and photovoltaic performance of PSCs.

Here, we introduce a formamidinium-based organic spacer, 4-trifluoromethyl benzamidine hydrochloride (TFPhFACl), as 2D capping layer atop 3D perovskite. $TFPhFA^+$ cations can coordinate with Pb–I octahedron, and form a 2D perovskite on top of 3D perovskite through Van der Waals interaction or hydrogen bonding. $TFPhFA^+$ with large polarity induces an electric field that accelerates the charge transport. The interfacial trap states are suppressed through chemical interaction between $TFPhFA^+$ and PbI_2 residues. Besides, the existence of Cl^- anions can induce recrystallization of 3D perovskite with less grain boundaries and improve the film quality. As a result, the photovoltaic performance of PSC treated with TFPhFACl exhibits a higher PCE of 24.0% compared with control device (21.9%). The devices show good air-stability and there is no decrease in efficiency after 1500 h.

2. Results and Discussion

The molecular structure of 4-trifluoromethyl benzamidine hydrochloride (TFPhFACl) comprises $-CF_3$, benzene ring, FA^+ cations, and Cl^- anions. The corresponding structure and the electrostatic surface potential map of $TFPhFA^+$ are shown in **Figure 1**a,b. Fluorine with the highest electronegativity can increase the molecular dipole moment.[15] As shown in Figure 1b, $-CF_3$ terminal group has negative charge while FA^+ exhibits positive charge. We calculated the dipole moment (μ_g) of $TFPhFA^+$ as high as 15.6 Debye. This value is consistent with published one that calculated for the fluorinated phenethylamine ($F–PEA^+$).[24] 2D perovskite capping layer was prepared by dissolving TFPhFACl into isopropanol (IPA), followed by spin-coating onto the as-prepared 3D perovskite substrates and heating at 100 °C for 3 min to promote the crystallization. The procedure is illustrated in Figure 1c. The perovskite films or devices treated with and without TFPhFACl are termed as control and TFPhFACl, respectively. The chemical interaction mechanism between $TFPhFA^+$ and 3D perovskite are depicted in Figure 1d. FA^+ functional group with positive charge is prone to fill the cation vacancies and coordinate with inorganic $[PbI_6]^{4-}$ octahedra through hydrogen bonding and Van der Waals force.[9] The formation of dipoles atop 3D perovskite can regulate the band alignment and facilitate the hole transport from perovskite to selective layer.[26,28] Moreover, the fluorinated terminal group with hydrophobic property can protect perovskite from the corrosion of water molecules, which is speculated to improve the device stability.[29] The increased hydrophobicity of TFPhFACl treated perovskite can be verified by measuring the water contact angle, as shown in Figure S1 (Supporting Information). With TFPhFACl treatment, the water contact angle increases from 45.09° to 54.32°, indicating the enhanced water-resistivity, which is beneficial for the device stability.

Surface dipoles can regulate the band alignment by changing the vacuum level of perovskite.[28] A positive dipole will upshift the local vacuum level and therefore increase the work function of top surface.[26] The energy level diagram of the 3D and 2D perovskite films were characterized by ultraviolet photoelectron spectroscopy (UPS) and shown in **Figure** 2a–c. The corresponding Tauc plots are illustrated in Figure S2 (Supporting Information). The work function of 3D perovskite and 2D films were calculated to be 4.57 and 4.77 eV, respectively. The valance band (VB) and conduction band (CB) for 2D and 3D perovskite were calculated to be −6.19 and −5.75, −3.27 and −4.21 eV, respectively. The 3D control perovskite exhibits a *n*–type nature while the 2D phase shows a weak *p*–type property. The formation of *n*–*p* type heterojunction can facilitate the carrier transport.[9,30,31] Kelvin probe force microscopy (KPFM) measurement was performed to characterize the surface contact potential of perovskite films that is shown in Figure 2d–f. Compared with the 3D perovskite, which exhibits a dark and

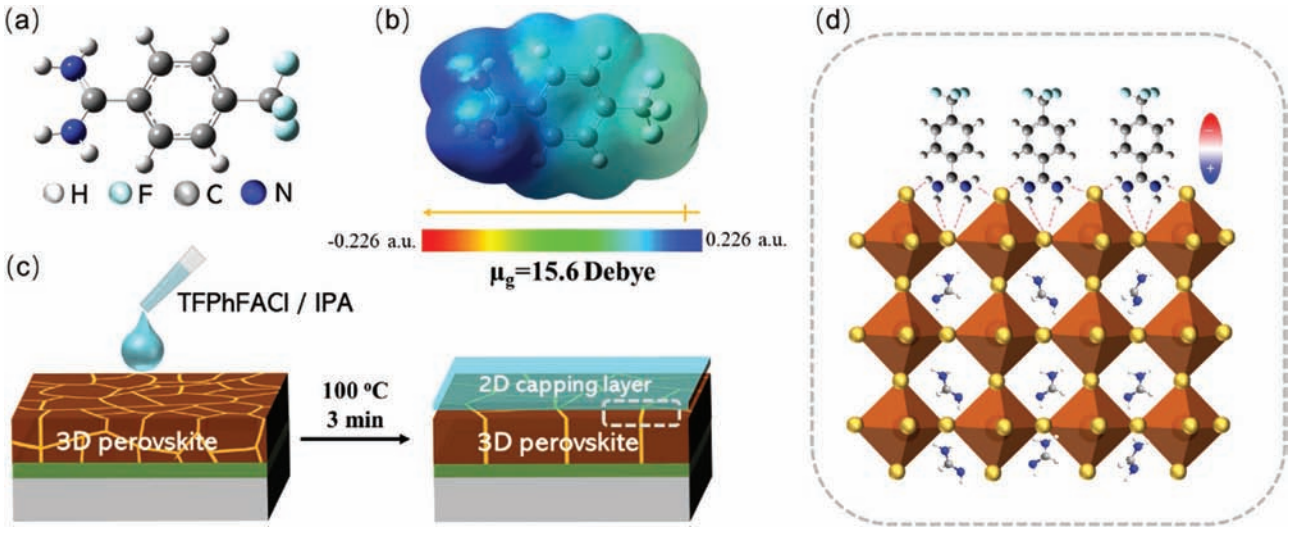

Figure 1. a) Molecular structure of $TFPhFA^+$ cation. b) Electrostatic potential map and dipole moment of $TFPhFA^+$ cation. c) Schematic diagram of surface treatment by TFPhFACl precursor to form 2D perovskite capping layer. d) Schematic diagram of the chemical interaction between $TFPhFA^+$ and Pb–I octahedron.

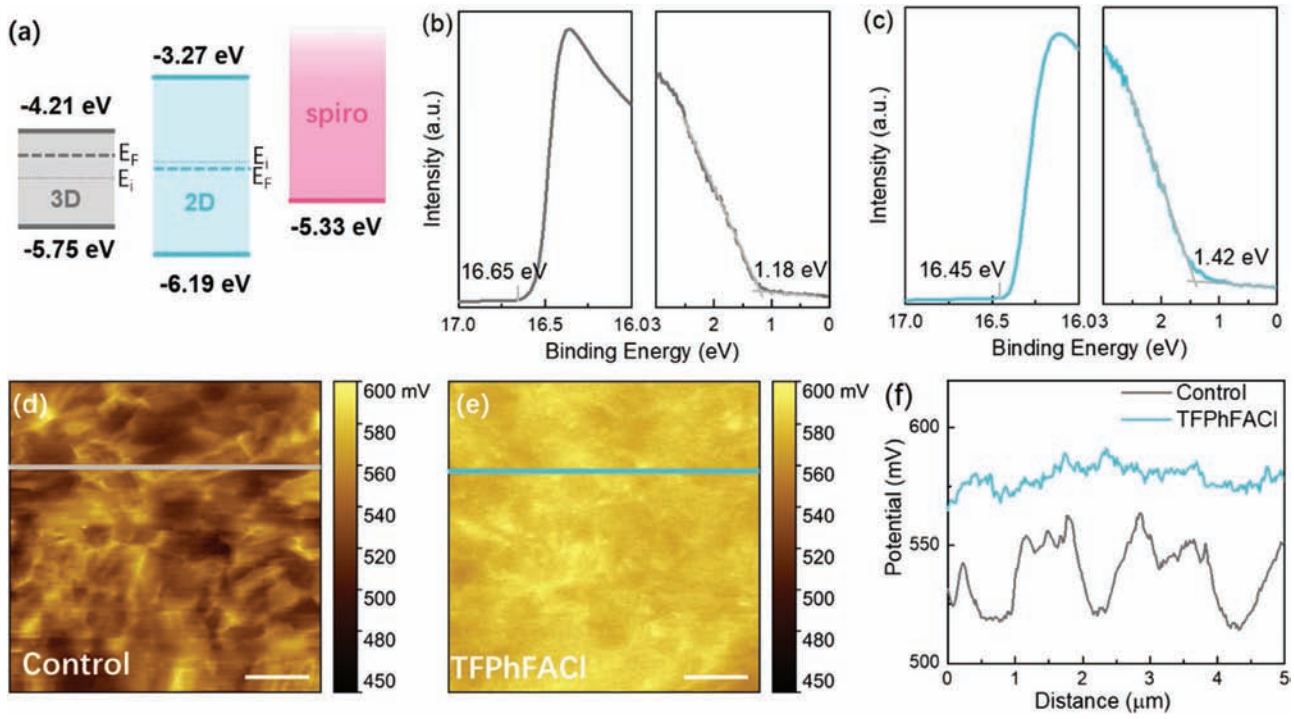

Figure 2. a) Energy level diagram of 3D perovskite, 2D perovskite and spiro-MeOTAD. b,c) UPS spectra of 3D and 2D perovskite. d,e) Surface potential maps of perovskite with and without TFPhFACl treatment. f) Potential amplitude along with the grey and cyan line shown in surface potential maps. The detected size is 5 × 5 μm, and the scale bar is 1 μm.

nonuniform potential distribution, the 2D/3D perovskite has a bright and uniform potential distribution. The high tip potential corresponds to the increase of work function after surface treatment that can be ascribed to the alignment of molecular dipoles induced by $TFPhFA^+$ cations.[32] Besides, these molecular dipoles are evenly distributed atop of 3D perovskite films in Figure 2e, since a smaller root mean surface potential of 5.95 mV is achieved for mixed 2D/3D perovskite while it is 15.58 mV for 3D perovskite. The formation of dipole layer by $TFPhFA^+$ helps promote the charge transport at interface between perovskite and selective layers.[25]

In order to further investigate the chemical interaction between TFPhFACl and 3D perovskite layers, X-ray photoelectron spectroscopy (XPS) were conducted and shown as **Figure 3**a–c. A clear and sharp F1s peak is observed for TFPhFACl treated sample in Figure 3a, verifying the successful incorporation of $TFPhFA^+$ cations. In Figure 3b, two distinct peaks at the binding energies of 143.3 and 138.55 eV refer to $Pb4f_{7/2}$ and $Pb4f_{5/2}$ satellites for 3D perovskite, corresponding to the Pb^{2+} ions in the Pb–I octahedra. Whereas both peaks downshift to lower binding energies of 142.6 and 137.85 eV with TFPhFACl treatment, indicating that the chemical reaction between the organic cations and Pb^{2+} ions. It is worth noting that two small peaks at the binding energies of 141.6 and 136.8 eV are observed for the control sample, which can be assigned to the Pb^0 defects.[33] It was reported that the Pb^0 impurities were the decomposition product of PbI_2 under X-ray irradiation.[34,35] The Pb^0 exists as deep level trap defects contributing to the nonradiative recombination and deteriorates the photovoltaic performances. The area ratio of Pb^0 at 141.65 eV decreases from 8.4% to 4.3% after TFPhFACl treatment. The suppressed Pb^0 peak is mainly due to the chemical reaction between $TFPhFA^+$ and PbI_2 residues. Similar phenomenon was also observed when use 2-CF_3-PEA^+ as large spacer cations.[33] In addition, the Pb–I bond length in 2D perovskite is slightly longer compared with FA-based perovskite, leading to the I 3d XPS spectra shift to a lower binding energy, as shown in Figure 3c. To confirm the chemical interaction between TFPhFACl and 3D perovskite, Fourier transform infrared spectroscopy (FTIR) analysis was performed using attenuated total reflection (ATR) mode, as shown in Figure 3d. For both control and TFPhFACl treated perovskites, strong absorption peaks observed at 1712 cm^{-1} corresponds to the stretching vibration of C=N in FA^+. The scissoring and anti-symmetry bending vibration of methyl ($-CH_3$) group from MA^+ appear at 1353 and 1471 cm^{-1}, respectively.[36] Besides, the spectrum of TFPhFACl powder is shown in Figure S3 (Supporting Information). The peak at 1679 cm^{-1} corresponding to the C=C stretching on benzene ring is observed both for TFPhFACl powder and TFPhFACl treated perovskite, indicating the successful incorporation of $TFPhFA^+$. At the same time, two small peaks at 1122 and 1319 cm^{-1} are observed in TFPhFACl powder relating to the $-CF_3$ stretching, and both peaks shift to high wavenumber of 1130 and 1324 cm^{-1} for 2D/3D perovskite.[37] These emerging peaks give strong evidence of the interaction between $TFPhFA^+$ cations with their surrounding elements.

The morphologies of perovskite films with and without TFPhFACl treatment were conducted by the scanning electron microscopy (SEM) to show the influence of surface treatment. The surface morphologies of 3D perovskite films

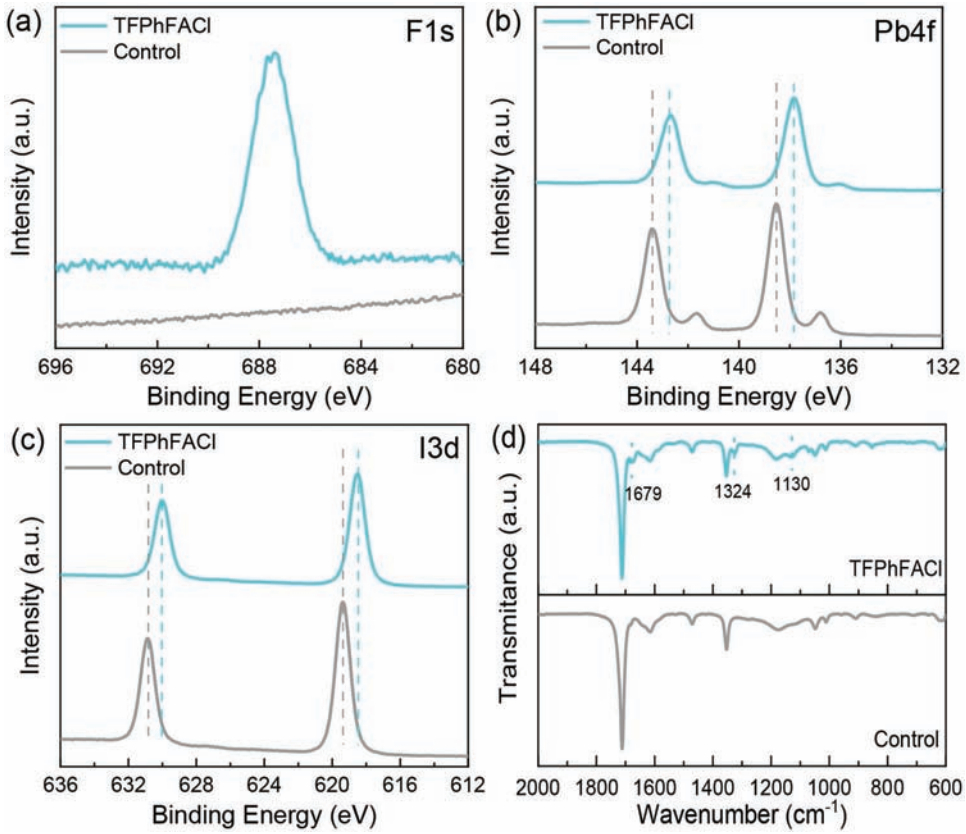

Figure 3. Characterization of chemical interaction between TFPhFACl and perovskite. a–c) XPS and d) FTIR spectra of perovskite films treated with and without TFPhFACl.

treated by TFPhFACl with different concentrations of 0, 2.5, 5, and 7.5 mg mL^{-1} are illustrated and shown in **Figure 4**a–d, and the corresponding cross-section images are shown in Figure 4e,f. Figure 4a shows the randomly distributed crystal grains for 3D perovskite film. When treating 3D perovskite with a low concentration of 2.5 mg mL^{-1}, some dark areas can be observed and ascribed to the accumulation of 2D perovskite at valley region. Besides, it is clearly observed in Figure 4b that the grain boundaries of 3D perovskite surface became more distinct than before, and the lamellar-structured regions were disappeared. This suggests that surface treatment of TFPhFACl induces the recrystallization of 3D perovskite. At high concentrations of 5 and 7.5 mg mL^{-1}, the surface morphologies of underlying 3D perovskite films are hardly distinguished due to the formation of mixed 2D/3D perovskite. We compared the cross-section images of the control and TFPhFACl treated perovskite films (5 mg mL^{-1}) in Figure 4e,f. In Figure 4f, cross-section image of the perovskite film treated with 5 mg mL^{-1} TFPhFACl became more smoother with less grain boundaries compared with the control one, suggesting the recrystallization of 3D perovskite again. We speculate that the recrystallization of 3D perovskite may be caused by Cl^- anions since chlorine sources such as MACl and $PbCl_2$ can effectively promote the growth and enhance the film quality of perovskites.[12,38] Atomic force microscopy (AFM) images for the 3D and 2D/3D composite perovskite were performed and shown in Figure S4 (Supporting Information). Compared with the 3D perovskite, the surface roughness of TFPhFACl treated perovskite film decreases from 36.7 to 22.1 nm, which is beneficial for the deposition of hole transport material. Besides, the reduced grain boundaries and surface roughness of mixed 2D/3D perovskite film are beneficial for the charge carriers transport and improvement of photovoltaic performance.

Grazing-incidence wide-angle X-ray scattering (GIWAXS) measurement is a powerful tool to characterize the crystallinity and crystal orientation of 2D/3D perovskites.[39] The penetration depth of the X-ray beam from surface to bulk is ~80 nm under the incident angle of 0.3°, allowing us to explore the near-surface region.[40] The GIWAXS patterns of the control and TFPhFACl treated perovskites are shown in **Figure 5**a,b, and the corresponding radically integrated intensity curves are shown in Figure 5c,d. The Debye–Scherrer diffraction rings at 8.5 and 10 nm^{-1} correspond to the PbI_2 signal and (110) plane of perovskite, respectively.[39] With TFPhFACl treatment, new diffraction rings at low q of 3–7 nm^{-1} are observed, indicating the successful formation of 2D perovskite on top of 3D perovskite. The integrated intensity of PbI_2 signal is slightly decreased, confirming that excess-PbI_2 was consumed through interacting with the organic spacer cation. Moreover, the 2D perovskite grows along with the out-of-plane direction, suggesting the vertical orientation, which benefits for the charge transport.[41]

The structural properties of 3D perovskite films with and without TFPhFACl treatment were further investigated by the X-ray diffraction (XRD) as shown in **Figure 6**a. The diffraction

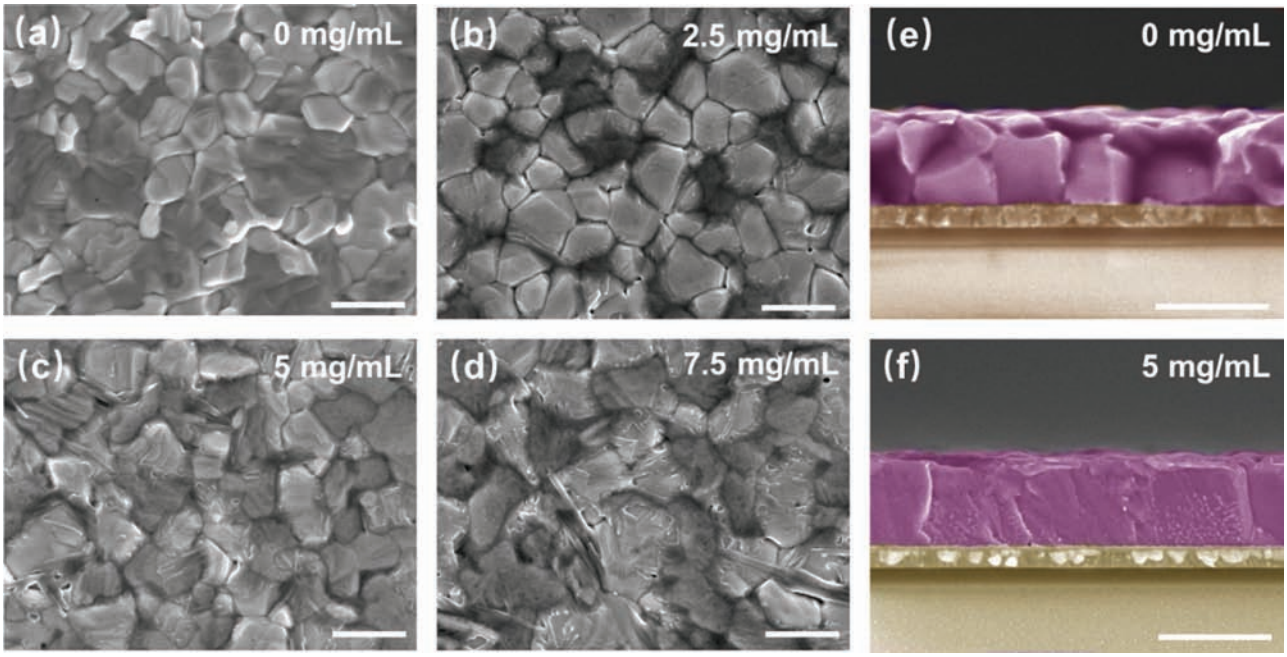

Figure 4. The morphology images of perovskite films treated with and without TFPhFACl. a–d) Surface images and e,f) cross-section images of perovskite films with different concentrations of TFPhFACl. The scale bar is 1 µm.

peak at 12.7° corresponds to the PbI_2 residues, which is suppressed after TFPhFACl treatment by forming 2D perovskite.[42] It is worth noting that we did not find the 2D diffraction peak below 10°, and this can be ascribed to the vertical growth of 2D perovskite.[41] The charge carrier recombination dynamics of 3D perovskite films before and after TFPhFACl treatment

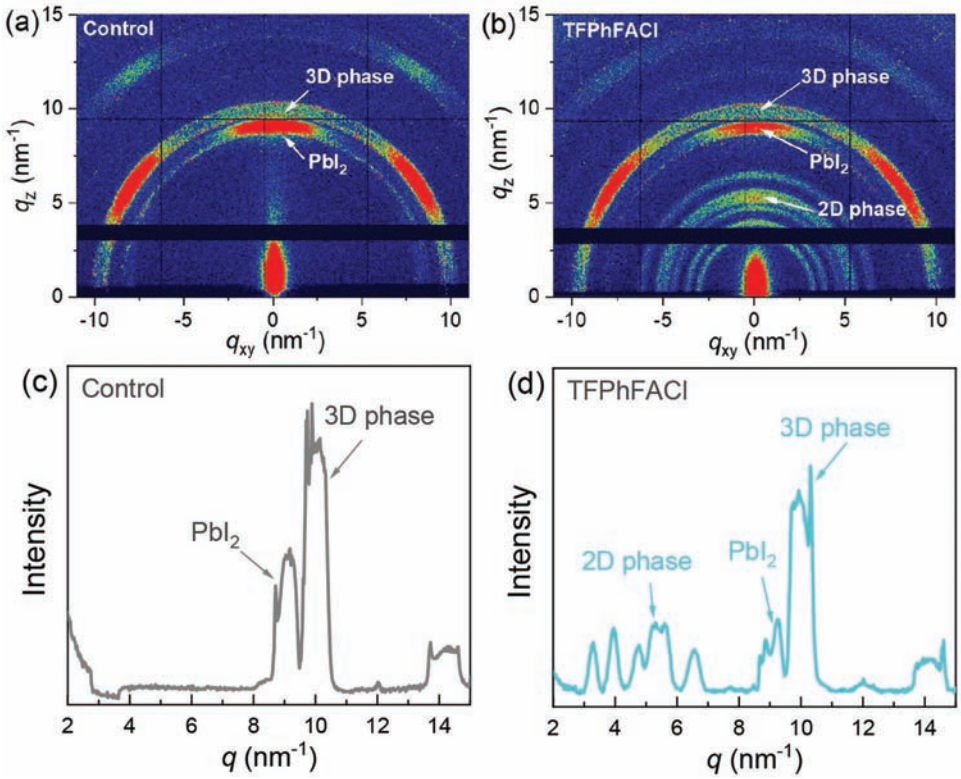

Figure 5. Structure properties of perovskite films. a,b) GIWAXS patterns of perovskite films treated with and without TFPhFACl. c,d) Corresponding radically integrated intensity of GIWAXS.

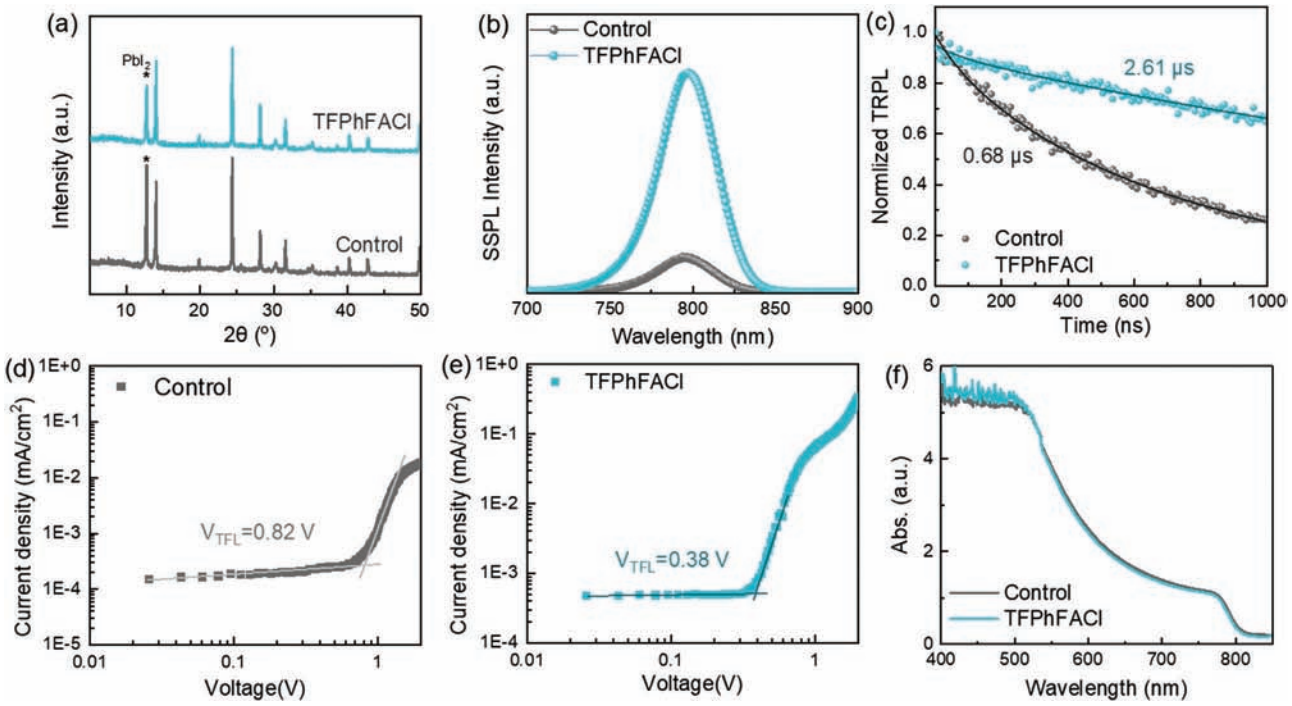

Figure 6. Characterization of perovskite films treated with and without TFPhFACl. a) XRD spectra of perovskite films. b) SSPL and c) TRPL of perovskite deposited on the glass substrates. d,e) SCLC curves of semi-devices with a structure of FTO/SnO_2/perovskites/PCBM/Au measured under dark condition. f) UV–visible absorbance of different perovskites.

were studied by steady-state photoluminescence (SSPL) and time resolved photoluminescence (TRPL) spectra. The perovskite films were deposited onto a bare glass with light incident from perovskite side. As shown in Figure 6b, the SSPL intensity of mixed 2D/3D perovskite film exhibits six times enhancement compared with the control sample, attributing to the decreased nonradiative recombination. The charge carrier lifetimes can be calculated from TRPL spectra as shown in Figure 6c and Table S1 (Supporting Information). TRPL spectra were fitted according to a biexponential decay function of $I(t) = I_0 + A_1\exp(-t/\tau_1) + A_2\exp(-t/\tau_2)$, where τ_1 and τ_2 are the lifetime constant.[43–45] The average lifetimes $\tau_{average}$, where $\tau_{average} = (A_1\tau_1^2 + A_2\tau_2^2)/(A_1\tau_1 + A_2\tau_2)$, are calculated to be 0.68 and 2.61 μs for the 3D and mixed 2D/3D perovskite films, respectively. The increased $\tau_{average}$ for the latter confirms the successful suppression of nonradiative recombination caused by trap defects.

Space charge limited current (SCLC) method was used to investigate the charge carrier dynamics of perovskites before and after TFPhFACl treatment.[16,24] The semi-devices were prepared with a structure of FTO/SnO_2/perovskite/PCBM/Au and measured under dark condition. The dark *I–V* curves are shown in Figure 6d,e for 3D and 2D/3D perovskite, respectively. The trap density (N_{trap}) of the perovskite can be calculated according to the formula of $N_{trap} = 2\varepsilon_0\varepsilon_r V_{TFL}\ qL^{-2}$, where ε_0 and ε_r are the vacuum dielectric constant and relative dielectric constant ($\varepsilon_r = 25$), q and L stand for the elementary charge (1.6×10^{-19} C) and thickness of perovskite (800 nm), respectively.[44] The calculated N_{trap} is 3.58×10^{15} cm^{-3} for 3D perovskite while it decreases to 1.38×10^{15} cm^{-3} for mixed 2D/3D perovskite. The reduction of trap defects indicates less nonradiative recombination and efficient charge transport, which are essential for the improvement of photovoltaic performance of PSCs. In Figure 6f, there is not much difference in light absorption for the control and TFPhFACl treated perovskite films. The formation of 2D capping layer does not contribute to the photocurrent due to its wide bandgap (≈2.9 eV, calculated from Figure S2b Supporting Information).

To investigate the influence of TFPhFACl induced capping layer on the photovoltaic performance, we fabricated the PSCs with an architecture of FTO/SnO_2/perovskite/spiro-MeOTAD/Au. The statistics of photovoltaic parameters are shown in Figure S5 (Supporting Information). The thickness of the perovskite layer is ~800 nm that is enough for light absorption.[46] The statistics of photovoltaic parameters of PSCs have an optimal concentration of 5 mg mL^{-1} for TFPhFACl treatment. *I–V* hysteresis of the control and TFPhFACl treated devices is negligible, as shown in Figure S6 (Supporting Information). The photovoltaic current–voltage *(J–V)* curves of the best performing PSCs for the control and TFPhFACl devices are shown in **Figure 7**a. The control PSC without TFPhFACl treatment delivers an efficiency of 21.9% with a J_{SC} of 25.49 mA cm^{-2}, a V_{OC} of 1.08 V and an FF of 79.77%. Compared with the control PSC, the champion TFPhFACl treated PSC delivers a much higher PCE of 24.0% with a J_{SC} of 25.42 mA cm^{-2}, a V_{OC} of 1.16 V, an FF of 81.26%. With TFPhFACl treatment, the suppressed nonradiative recombination together with the acceleration of charge transport induced by surface dipoles contribute to the improvement in V_{OC} and FF. Figure 7b,c show the statistical V_{OC}s and PCEs for two kinds of PSCs. The average V_{OC} increases from 1.05 V for the control PSCs to 1.15 V for the TFPhFACl treated PSCs, resulting in the PCE increased from 19.7 to 22.4%. J_{SC}s for

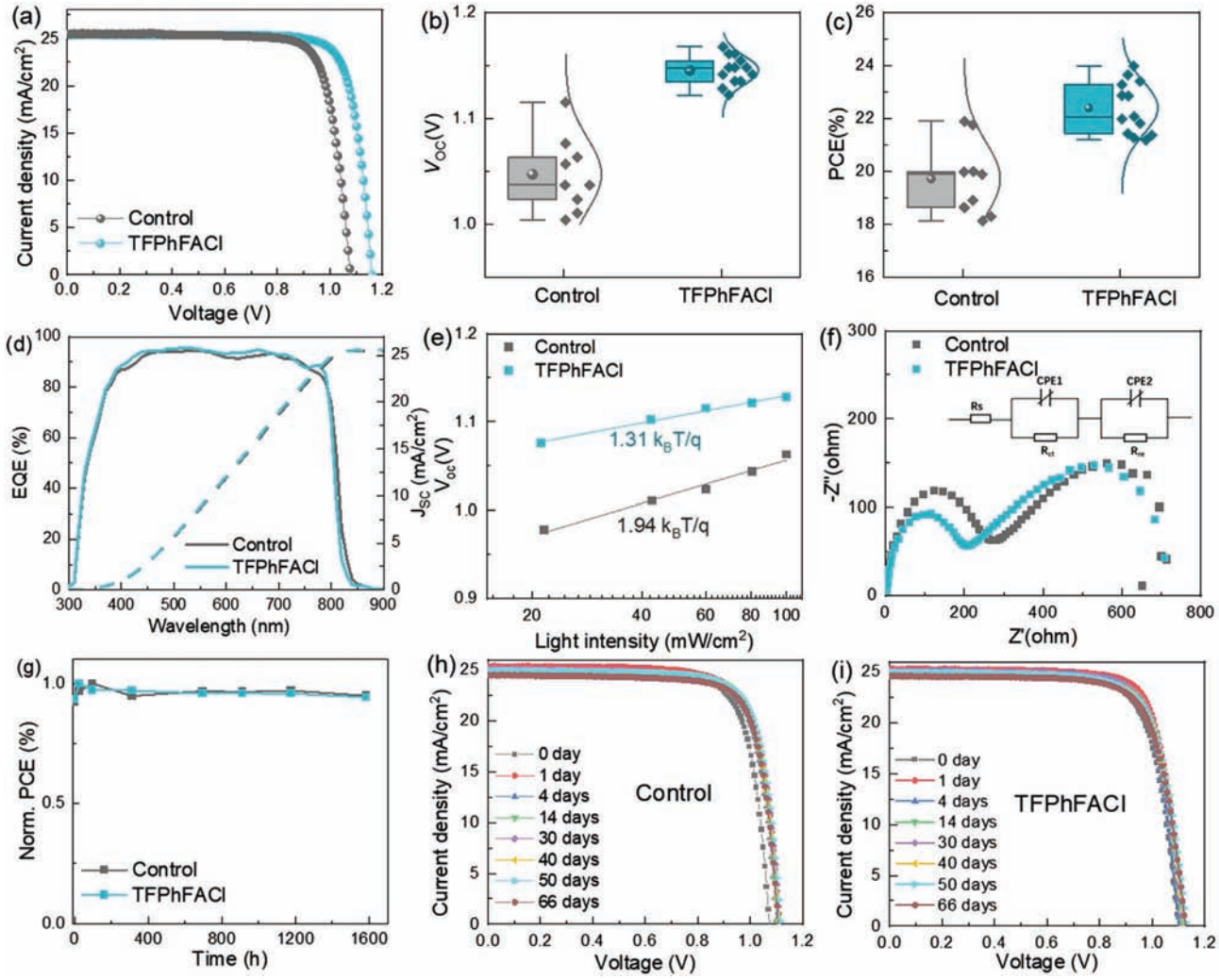

Figure 7. Characterization of PSCs. a–c) photovoltaic performance of PSCs including *J–V* curves, statistics of V_{OC}s and PCEs. d) External quantum efficiency (EQE) spectra, e) light-dependent V_{OC} changes and f) EIS of PSCs. g–i) Air stability of the PSCs measured under the humidity of ≈40% and stored in a dry box with a humidity below 20%.

two devices are similar since there is no big difference in light absorption and integrated J_{SC}s based on the external quantum efficiency (EQE) are shown in Figure 7d.

Figure 7e illustrates the dependence of V_{OC} on the light intensities to investigate the charge extraction and recombination kinetics of PSCs before and after TFPhFACl treatment. The relationship between V_{OC} and light intensity follows the equation of $V_{OC} = nk_BT\ln(I)/q + C$, where n is the ideal factor, k_B is the Boltzmann constant, T is the temperature, q is the elementary charge and C is the constant.[47] Diode ideality factor n ranges from 1 to 2. When $n = 1$, electrons and holes exhibit bimolecular recombination; when $n = 2$, electrons and holes exhibit a monomolecular recombination (Shockley–Read–Hall (SRH) recombination). By linear fitting the V_{OC} under different light intensities, n is calculated to be 1.94 for the control PSC and 1.31 for TFPhFACl treated PSC, respectively. The reduced n for the latter indicates suppressed trap-assisted SRH recombination that contributes to the increase of V_{OC} and FF. Electrochemical impedance spectroscopy (EIS) is further studied to understand the interfacial charge transfer and carrier recombination. As shown in the Figure 7f, the Nyquist plots of PSCs were measured under a bias voltage of 0.8 V with the frequency from 1 MHz to 0.1 Hz and fitted according to the inserted equivalent circuit. Two semi-arcs of Nyquist plots are clearly observed for all samples. Semicircle in the high frequency region relates to the charge transport resistance (R_{ct}) and the semicircle in the low frequency region correspond to the recombination resistance (R_{rec}). After surface treatment, the series resistance (R_s) is slightly decreased from 4.89 to 4.02 Ω. There is little difference in R_{ct}. Larger R_{rec} (224 Ω) for the TFPhFACl treated PSC was obtained compared with the control PSC (169.6 Ω), indicating the restrained nonradiative recombination at the interface.

The photovoltaic performances were continuously monitored to check the stability of PSCs as shown in Figure 7g–i. The unencapsulated devices were stored in a dry box with a humidity below 20% and measured under the humidity of 40–50%. The normalized efficiency change is shown in Figure 7g and

the corresponding *J–V* curves are shown in Figure 7h,i. Both devices show good stability after 1500 h storage and the PCEs shows no decrease, indicating the good air stability.

3. Conclusion

In this work, TFPhFACl was applied as organic spacer cation to construct 2D perovskite atop 3D perovskite for the first time. We show that the TFPhFACl molecule with different chemical groups has multifunctional passivation effects on the 3D perovskite films, and thus affects the charge carrier transport and recombination of PSCs. First, the large polarity of $TFPhFA^+$ cations forms a dipole layer at top surface that facilitates the charge transport from perovskite to selective layer. Second, the nonradiative recombination is suppressed not only through the chemical interaction between $TFPhFA^+$ and PbI_2 by forming 2D perovskite, but also through the recrystallization of 3D perovskite induced by Cl^- anions. These synergistic effects are responsible for the improvement of photovoltaic performance of PSCs. As a result, the PCE of PSC with TFPhFACl treatment was improved from 21.9% to 24.0% mainly due to the increase in FF and V_{OC}. There is no decrease in efficiency for TFPhFACl treated PSCs after 1500 h stored in a dry box indicating the good air-stability. This work provides a facile and effective way to improve the efficiency of PSCs. The utilization of TFPhFACl enlarges the category of organic spacer cation for surface passivation and constructing 2D/3D heterojunction, which can be also applied to other perovskite-based electronical devices. More importantly, it provides a new perspective for choosing and designing an efficient organic spacer molecule for interface engineering.

4. Experimental Section

Materials: The 15 wt.% SnO_2 colloidal solution was purchased from Alfa Asear. PbI_2 (99.99%) was purchased from Tokyo Chemical Industry (TCI). Methylammonium iodide (CH_3NH_3I, MAI), formamidinium iodide ($CH(NH_2)_2I$, FAI), methylammonium chloride (CH_3NH_3Cl, MACl), 4-tert-butylpyridine (tBP), li-bis(trifluoromethanesulfonyl)imid (LI-TFSI), and 2,2′,7,7′-Tetrakis[N,N-di(4-methoxy phenyl)amino]-9,9′-spirobifluorene (spiro-MeOTAD) were purchased from Xi'an Polymer Light Technology Corporation. 4-Trifluoromethyl benzamidine hydrochloride was purchased from Aladdin. *N*, *N* dimethylformamide (DMF), dimethyl sulfoxide (DMSO), isopropanol (IPA), acetonitrile (ACN), and chlorobenzene (CB) were purchased from Sigma–Aldrich. All chemicals were used without further purification.

Device Fabrication: Fluorine-doped tin oxide (FTO) glasses with a sheet resistance of 8 Ω sq^{-1} were ultrasonicated and cleaned with detergent, ethanol and acetone and DI-water for 10 min in sequence. Before depositing SnO_2 electron transport layer (ETL), the precleaned FTO substrates were subjected to UVO treatment for 10 min. For ETL deposition, water-diluted SnO_2 precursor solution (with a volume ratio of V_{H2O}:V_{SnO2} = 4:1) was spin-coated onto precleaned FTO substrates at 4000 rpm for 30 s, followed by annealing at 150 °C for 30 min. The perovskite film was prepared by a two-step deposition method according to the published report.[48,49] PbI_2 (1.5 M) was dissolved in a mixed solvent of DMF/DMSO with a volume ratio of 9:1. The PbI_2 precursor solution was spin-coated at 1500 rpm for 30 s and preheated at 70 °C for 1 min. The organic ammonium salt solution containing 90 mg FAI, 6.4 mg MAI, 9 mg MACl, and 1 mL IPA was spin-coated onto the as-prepared PbI_2 films, followed by annealing at 150 °C for 15 min in air to promote the crystallization of perovskite. For 2D capping layer, 4-trifluoromethyl benzamidine hydrochloride was dissolved in IPA with different concentrations including 0, 2.5, 5, and 7.5 mg mL^{-1}, followed by spin-coating at 4000 rpm for 30 s. Post annealing at 100 °C for 3 min was necessary to promote the crystallization of 2D perovskite. For pure $(TFPhFA)_2PbI_4$ 2D perovskite, 44.8 mg TFPhFACl, and 46.1 mg PbI_2 was dissolved in 400 µL DMF and 100 µL DMSO, followed by spin-coating at 4000 rpm for 30 s and heating at 100 °C for 10 min. Finally, hole transport material including 72 mg spiro-MeOTAD, 27 µL tBP, and 15 µL Li-TFSI (520 mg mL^{-1} in ACN) was spin-coated at 4000 rpm for 30 s on top of perovskite layers, and 80 nm Au was thermal-evaporated to obtain the PSCs.

Computational Methods: All calculations were done using the Gaussian 16 program. Geometry optimization calculations for $TFPhFA^+$ were performed by using b3lyp 6-311+g(d) method.[50] The electrostatic potential (ESP) of the model were analyzed using Gaussian view.

Characterization: The morphologies of perovskite films were characterized by the scanning electron microscopy (SU8010, Hitachi) and atomic force microscopy (FMNanoview 1000). X-ray photoelectron spectroscopy (XPS) was characterized by an ESCALAB 250Xi (Thermo Fisher Scientific) system equipped with Al K_α radiation. Ultraviolet photoelectron spectroscopy (UPS) was performed using a ESCLAB Xi+ system equipped with a He I (21.22 eV) radiation source. Grazing-incidence wide-angle x-ray scattering (GIWAXS) was performed with an incident angle of 0.3° using a Xeuss 3.0 system (Xenocs) equipped with a Eiger2R 1 M detector. The GIWAXS pattern was fitted using a Fit2D software. X-ray diffraction spectra were carried out by an X-ray diffractometer (D8 Advance, Bruker). Steady-state and the time-resolved photoluminescence (PL) were performed by a FLS980 fluorescence spectrometer (Edinburgh Instrument) equipped with a 450 W Xe lamp and a picosecond-pulsed diode 405 nm laser (EPL-405). The current–voltage (*J–V*) photovoltaic performances were measured with the scanning rate of 0.165 V s^{-1} under AM 1.5 illumination using a Keithley 2400 source meter with an aperture area of 0.1 cm^2. The external quantum efficiency (EQE) of PSCs was achieved using a QE-R system (Enli Tech.). The charge transport dynamics of PSCs were analyzed using a Zahner Zennium electrochemical workstation and fitted by a ZView software.

Supporting Information

Supporting Information is available from the Wiley Online Library or from the author.

Acknowledgements

X.Y. and X.Z. contributed equally to this work. This work was supported partially by National Natural Science Foundation of China (Grant nos. 51972110, 52102245, and 52072121), Beijing Natural Science Foundation (2222076, 2222077), project of State Key Laboratory of Alternate Electrical Power System with Renewable Energy Sources (LAPS202114), Huaneng Group Headquarters Science and Technology Project (HNKJ20-H88), the Fundamental Research Funds for the Central Universities (2020MS023, 2020MS028), and the NCEPU "Double First-Class" Program.

Conflict of Interest

The authors declare no conflict of interest.

Data Availability Statement

Research data are not shared.

Keywords

2D perovskites, charge transport, dipole molecules, efficiency, nonradiative recombinations

Received: August 27, 2022
Revised: October 20, 2022
Published online:

[1] J. Burschka, N. Pellet, S.-J. Moon, R. Humphry-Baker, P. Gao, M. K. Nazeeruddin, M. Grätzel, *Nature* **2013**, *499*, 316.
[2] M. Liu, M. B. Johnston, H. J. Snaith, *Nature* **2013**, *501*, 395.
[3] H.-S. Kim, C.-R. Lee, J.-H. Im, K.-B. Lee, T. Moehl, A. Marchioro, S.-J. Moon, R. Humphry-Baker, J.-H. Yum, J. E. Moser, M. Grätzel, N.-G. Park, *Sci. Rep.* **2012**, *2*, 591.
[4] N. R. E. L., (NREL), https://www.nrel.gov/pv/cell-efficiency.html (accessed: July 2022).
[5] Y. Li, H. Xie, E. L. Lim, A. Hagfeldt, D. Bi, *Adv. Energy Mater.* **2022**, *12*, 2102730.
[6] C. M. Wolff, P. Caprioglio, M. Stolterfoht, D. Neher, *Adv. Mater.* **2019**, *31*, 1902762.
[7] M. A. Mahmud, T. Duong, J. Peng, Y. Wu, H. Shen, D. Walter, H. T. Nguyen, N. Mozaffari, G. D. Tabi, K. R. Catchpole, K. J. Weber, T. P. White, *Adv. Funct. Mater.* **2022**, *32*, 2009164.
[8] J. Gong, M. Hao, Y. Zhang, M. Liu, Y. Zhou, *Angew. Chem., Int. Ed.* **2022**, *61*, e202112022.
[9] G. Wu, R. Liang, M. Ge, G. Sun, Y. Zhang, G. Xing, *Adv. Mater.* **2022**, *34*, 2105635.
[10] X. Zhao, T. Liu, Y. L. Loo, *Adv. Mater.* **2022**, *34*, 2105849.
[11] I. C. Smith, E. T. Hoke, D. Solis-Ibarra, M. D. McGehee, H. I. Karunadasa, *Angew. Chem., Int. Ed.* **2014**, *53*, 11232.
[12] K. Odysseas Kosmatos, L. Theofylaktos, E. Giannakaki, D. Deligiannis, M. Konstantakou, T. Stergiopoulos, *Energy Environ. Mater.* **2019**, *2*, 79.
[13] J. W. Xiao, L. Liu, D. Zhang, N. De Marco, J. W. Lee, O. Lin, Q. Chen, Y. Yang, *Adv. Energy Mater.* **2017**, *7*, 1700491.
[14] Y. Dong, D. Lu, Z. Xu, H. Lai, Y. Liu, *Adv. Energy Mater.* **2020**, *10*, 2000694.
[15] Q. Li, Y. Dong, G. Lv, T. Liu, D. Lu, N. Zheng, X. Dong, Z. Xu, Z. Xie, Y. Liu, *ACS Energy Lett.* **2021**, *6*, 2072.
[16] X. Li, W. Hu, Y. Shang, X. Yu, X. Wang, W. Zhou, M. Wang, Q. Luo, C. Q. Ma, Y. Lu, S. Yang, *J. Energy Chem.* **2022**, *66*, 680.
[17] T. Liu, J. Guo, D. Lu, Z. Xu, Q. Fu, N. Zheng, Z. Xie, X. Wan, X. Zhang, Y. Liu, Y. Chen, *ACS Nano* **2021**, *15*, 7811.
[18] Y. Zheng, T. Niu, X. Ran, J. Qiu, B. Li, Y. Xia, Y. Chen, W. Huang, *J. Mater. Chem. A* **2019**, *7*, 13860.
[19] M. Safdari, P. H. Svensson, M. T. Hoang, I. Oh, L. Kloo, J. M. Gardner, *J. Mater. Chem. A* **2016**, *4*, 15638.
[20] S. Deng, E. Shi, L. Yuan, L. Jin, L. Dou, L. Huang, *Nat. Commun.* **2020**, *11*, 664.
[21] L. Chen, Q. Chen, C. Wang, Y. Li, *J. Am. Chem. Soc.* **2020**, *142*, 18281.
[22] Z. Ren, X. Xiao, R. Ma, H. Lin, K. Wang, X. W. Sun, W. C. H. Choy, *Adv. Funct. Mater.* **2019**, *29*, 1905339.
[23] F. Ansari, E. Shirzadi, M. Salavati-Niasari, T. Lagrange, K. Nonomura, J. H. Yum, K. Sivula, S. M. Zakeeruddin, M. K. Nazeeruddin, M. Grätzel, P. J. Dyson, A. Hagfeldt, *J. Am. Chem. Soc.* **2020**, *142*, 11428.
[24] H. Su, L. Zhang, Y. Liu, Y. Hu, B. Zhang, J. You, X. Du, J. Zhang, X. Ren, J. Gou, S. (Frank) Liu, *Nano Energy* **2022**, *95*, 106965.
[25] S. Tan, N. Zhou, Y. Chen, L. Li, G. Liu, P. Liu, C. Zhu, J. Lu, W. Sun, Q. Chen, H. Zhou, *Adv. Energy Mater.* **2019**, *9*, 1803024.
[26] J. Duan, M. Wang, Y. Wang, J. Zhang, Q. Guo, Q. Zhang, Y. Duan, Q. Tang, *ACS Energy Lett.* **2021**, *6*, 2336.
[27] Y. Qiu, J. Liang, Z. Zhang, Z. Deng, H. Xu, M. He, J. Wang, Y. Yang, L. Kong, C. C. Chen, *J. Phys. Chem. C* **2021**, *125*, 1256.
[28] L. Canil, T. Cramer, B. Fraboni, D. Ricciarelli, D. Meggiolaro, A. Singh, M. Liu, M. Rusu, C. M. Wolff, N. Phung, Q. Wang, D. Neher, T. Unold, P. Vivo, A. Gagliardi, F. De Angelis, A. Abate, *Energy Environ. Sci.* **2021**, *14*, 1429.
[29] A. Bala, V. Kumar, *ACS Appl. Energy Mater.* **2021**, *4*, 1860.
[30] P. Cui, D. Wei, J. Ji, H. Huang, E. Jia, S. Dou, T. Wang, W. Wang, M. Li, *Nat. Energy* **2019**, *4*, 150.
[31] P. C. Huang, S. K. Huang, T. C. Lai, M. C. Shih, H. C. Hsu, C. H. Chen, C. C. Lin, C. H. Chiang, C. Y. Lin, K. Tsukagoshi, C. W. Chen, Y. P. Chiu, S. F. Tsay, Y. C. Wang, *Nano Energy* **2021**, *89*, 106362.
[32] S. Zhao, J. Xie, G. Cheng, Y. Xiang, H. Zhu, W. Guo, H. Wang, M. Qin, X. Lu, J. Qu, J. Wang, J. Xu, K. Yan, *Small* **2018**, *14*, 1803350.
[33] J. Zhou, M. Li, S. Wang, L. Tan, Y. Liu, C. Jiang, X. Zhao, L. Ding, C. Yi, *Nano Energy* **2022**, *95*, 107036.
[34] J. D. McGettrick, K. Hooper, A. Pockett, J. Baker, J. Troughton, M. Carnie, T. Watson, *Mater. Lett.* **2019**, *251*, 98.
[35] J. Liang, X. Hu, C. Wang, C. Liang, C. Chen, M. Xiao, J. Li, C. Tao, G. Xing, R. Yu, W. Ke, G. Fang, *Joule* **2022**, *6*, 816.
[36] P. L. Qin, G. Yang, Z. W. Ren, S. H. Cheung, S. K. So, L. Chen, J. Hao, J. Hou, G. Li, *Adv. Mater.* **2018**, *30*, 17061126.
[37] H. Li, J. Song, W. Pan, D. Xu, W. an Zhu, H. Wei, B. Yang, *Adv. Mater.* **2020**, *32*, 202003790.
[38] H. Li, J. Zhou, L. Tan, M. Li, C. Jiang, S. Wang, X. Zhao, *Sci. Adv.* **2022**, *8*, eabo7422.
[39] Y. Zhong, G. Liu, Y. Su, W. Sheng, L. Gong, J. Zhang, L. Tan, Y. Chen, *Angew. Chem.* **2022**, *134*, e202114588.
[40] B. wook Park, N. Kedem, M. Kulbak, D. Y. Lee, W. S. Yang, N. J. Jeon, J. Seo, G. Kim, K. J. Kim, T. J. Shin, G. Hodes, D. Cahen, S. Il Seok, *Nat. Commun.* **2018**, *9*, 3301.
[41] H. Lai, B. Kan, T. Liu, N. Zheng, Z. Xie, T. Zhou, X. Wan, X. Zhang, Y. Liu, Y. Chen, *J. Am. Chem. Soc.* **2018**, *140*, 11639.
[42] R. Azmi, E. Ugur, A. Seitkhan, F. Aljamaan, A. S. Subbiah, J. Liu, G. T. Harrison, M. I. Nugraha, M. K. Eswaran, M. Babics, Y. Chen, F. Xu, T. G. Allen, A. Rehman, C. Wang, T. D. Anthopoulos, U. Schwingenschlögl, M. De Bastiani, E. Aydin, S. De Wolf, *Science* **2022**, *376*, 73.
[43] H. Zhang, J. Cheng, F. Lin, H. He, J. Mao, K. S. Wong, A. K. Y. Jen, W. C. H. Choy, *ACS Nano* **2016**, *10*, 1503.
[44] J. Chen, X. Zhao, S. G. Kim, N. G. Park, *Adv. Mater.* **2019**, *31*, 1902902.
[45] X. Zhao, J. Chen, N.-G. Park, *Sol. RRL* **2019**, *3*, 1800339.
[46] N.-G. Park, *Mater. Today* **2015**, *18*, 65.
[47] S. R. Cowan, A. Roy, A. J. Heeger, *Phys. Rev. B: Condens. Matter Mater. Phys.* **2010**, *82*, 245207.
[48] Q. Jiang, Z. Chu, P. Wang, X. Yang, H. Liu, Y. Wang, Z. Yin, J. Wu, X. Zhang, J. You, *Adv. Mater.* **2017**, *29*, 1703852.
[49] Q. Jiang, L. Zhang, H. Wang, X. Yang, J. Meng, H. Liu, Z. Yin, J. Wu, X. Zhang, J. You, *Nat. Energy* **2016**, *2*, 16177.
[50] Y. Zhao, D. G. Truhlar, *Theor. Chem. Acc.* **2008**, *120*, 215.